Earth and Planetary Science Letters 541 (2020) 116291

Contents lists available at ScienceDirect

Earth and Planetary Science Letters

www.elsevier.com/locate/epsl

Origin and evolution of fault-controlled hydrothermal dolomitization fronts: A new insight

Ardiansyah Koeshidayatullah [a,*,1], Hilary Corlett [b], Jack Stacey [a], Peter K. Swart [c], Adrian Boyce [d], Cathy Hollis [a]

[a] School of Natural Sciences, Williamson Building, Oxford Road University of Manchester, M13 9PL, UK
[b] MacEwan University, Alberta, T5J 4S2, Canada
[c] Rosenstiel School of Marine and Atmospheric Sciences, University of Miami, 33149, USA
[d] Scottish Universities Environmental Research Centre, Glasgow, G75 0QF, UK

ARTICLE INFO

Article history:
Received 2 October 2019
Received in revised form 12 April 2020
Accepted 16 April 2020
Available online 12 May 2020
Editor: I. Halevy

Keywords:
dolomitization fronts
hydrothermal
Mg/Ca ratio
recrystallization
retreat
self-limiting

ABSTRACT

Dolomitization is one of the most significant diagenetic reactions in carbonate systems, occurring where limestone ($CaCO_3$) is replaced by dolomite ($CaMg(CO_3)_2$) under a wide range of crystallization temperatures and fluids. The processes governing its formation have been well studied, but the controls on the position of dolomitization fronts in ancient natural settings, particularly in a fault-controlled hydrothermal system (HTD), have received remarkably little attention. Hence, the origin and evolution of HTD dolomitization fronts in the stratigraphic record remain enigmatic. Here, a new set of mineralogical and geochemical data collected from different transects in a partially dolomitized Cambrian carbonate platform in western Canada are presented to address this issue. Systematic patterns of sudden decrease in the magnesium content (mol% $MgCO_3$) and increase in porosity were observed towards the margin of the body. Furthermore, fluid temperatures are cooler and $\delta^{18}O_{water}$ values are less positive at the dolomitization front than within the core of the body. These changes coincide with a change from poorly ordered, planar-e dolomite with multiple crystal zonations at the margin, to an unzoned, well-ordered, interlocking mosaic of planar-s to nonplanar dolomite in the core of the body.

These phenomena are hypothesized to reflect dynamic, self-limiting processes in the formation and evolution of HTD dolomitization fronts through (i) plummet of dolomitization potential at the head of dolomitizing fluids due to progressive consumption of magnesium and fluid cooling; and (ii) retreat of dolomitization fronts towards the fluid source during subsequent recrystallization of the dolomite body, inboard of the termination, once overdolomitization took place. This new insight illustrates how dolomitization fronts can record the oldest phase of dolomitization, instead of the youngest as is often assumed. Formation of porosity is interpreted to occur as the result of acidification-induced grain leaching during the development of dolomitization fronts. This mechanism, coupled with retrogradation of dolomitization fronts, may help to explain the apparent enhancement of porosity in proximity to dolomitization fronts.

1. Introduction

The presence of dolomite bodies and their associated depositional and diagenetic contacts with the adjacent limestone (i.e. dolomitization fronts) have been widely reported in the literature across a range of dolomitized platforms, using field studies (e.g. Wilson et al., 1990; Nader et al., 2007; Budd and Mathias, 2015; Hollis et al., 2017; Al-Ramadan et al., 2019) and numerical simulations (e.g. Xiao and Jones, 2007; Yapparova et al., 2017). While dolomitization fronts occur in all dolomitized carbonates, they are most easily described in fault-controlled hydrothermal (HTD) systems because they are defined by an obvious color contrast with the adjacent limestone (e.g. Sharp et al., 2010; Merino and Canals, 2011).

The position of dolomitization fronts is commonly ascribed to changes in rock physical properties, such as a reduction in

* Corresponding author.
E-mail address: ardikoes@stanford.edu (A. Koeshidayatullah).
[1] Present address: Geological Sciences Department, Stanford University, Palo Alto, 94305, USA.

https://doi.org/10.1016/j.epsl.2020.116291

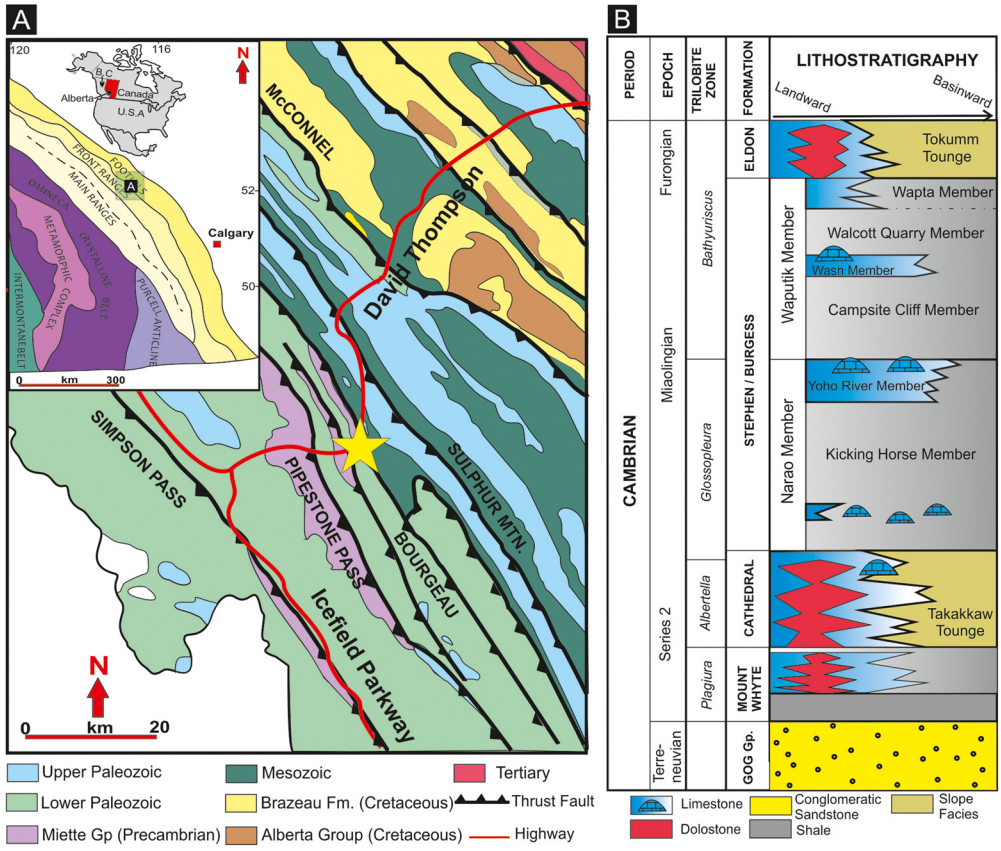

Fig. 1. (A) Geological map of the study area showing the distribution of Palaeozoic to Mesozoic sedimentary sequences and thrust faults in the Front Ranges, WCSB (modified after Gabrielse, 1991). The study location (yellow star) is bounded by two major NW-SE thrust faults, Bourgeau and Pipestone Pass. (B) General Lithostratigraphy of the study area and surroundings (modified after Collom et al., 2009). (For interpretation of the colors in the figure(s), the reader is referred to the web version of this article.)

rock permeability at the termination point, or discontinuation of fluid supply and drive mechanism. Wilson et al. (1990) ascribed the position of dolomitization fronts to magnesium depletion due to cooling of the fluid. Numerical simulation by Merino and Canals (2011) further examined the formation of high temperature dolomitization fronts and proposed that the governing process was self-accelerating and induced by the release of Ca^{2+} during replacement. Recently, Budd and Mathias (2015) interpreted self-organization during dolomitization as a possible control on dolomite body termination in Miocene carbonates, based on the discrepancy in statistical trends between dolomite and limestone. Furthermore, Kondratiuk et al. (2015) proposed that the formation of porosity at dolomitization fronts occurred through synchronization between dissolution and precipitation fronts.

These previous studies have laid an exceptional foundation by which to understand the potential mechanisms for the formation of dolomitization fronts, and the associated changes in rock physical properties. However, only a few studies have investigated the formation and evolution of ancient dolomitization fronts in natural HTD systems (e.g. Wilson et al., 1990; Nader et al., 2007; Budd and Mathias, 2015). Therefore, the actual processes governing the termination of HTD dolomite bodies remains poorly understood. This study aims to address this knowledge gap through systematic high-resolution sampling and analysis of several transects of Cambrian HTD dolomitization fronts in the Western Canada Sedimentary Basin (WCSB) (Fig. 1). The results will be compared with other published field, numerical and experimental studies to determine (i) the influence of physical-chemical changes of dolomitizing fluids in controlling the extend of HTD dolomitization (ii) how the fluid flow evolved through time and impacted the position of dolomitization fronts and (iii) what controls the spatio-temporal porosity distribution and preservation within HTD dolomite bodies.

2. Geological framework

2.1. Basin and stratigraphy

The WCSB is a mature hydrocarbon province that is situated within a complex tectonic basin, influenced by Precambrian-aged transform faults and Mesozoic fold-thrust belt deformation (Wright et al., 1994) (Fig. 1). In general, this basin can be divided into two major tectonostratigraphic units. A Palaeozoic carbonate-dominated system, developed on a passive margin, formed following reactivation of Precambrian faults during rifting in the Cambrian (Collom et al., 2009). The Cambrian sequence is dominated by successions of carbonate platforms and overlying shales that persisted throughout the Cambrian. In the southern and central Rockies (e.g. Whirlpool Point), shale intervals, such as the Mount Whyte Formation, were more carbonate rich. Regionally, all of the Cambrian strata transitioned from carbonate rich to shale rich from west to east (Pugh, 1973). Inundation of Laurentia during the Devono-Carboniferous resulted in an epeiric sea that stretched across northeastern British Columbia, Alberta, and into Saskatchewan, with the basin undergoing fault reactivation related to Antler Orogeny-aged tectonism (Hauck et al., 2017). Since the Mesozoic, siliciclastic sedimentation has dominated the basin, associated with the development of a foreland basin during the Laramide Orogeny (Pană and van der Pluijm, 2015). Here, we focus on the well-exposed, partially dolomitized Cambrian carbonate platform of the Mount Whyte Formation (Fig. 1B). In the Whirlpool Point locality (Fig. 1A), the dolomite bodies are mostly parallel to

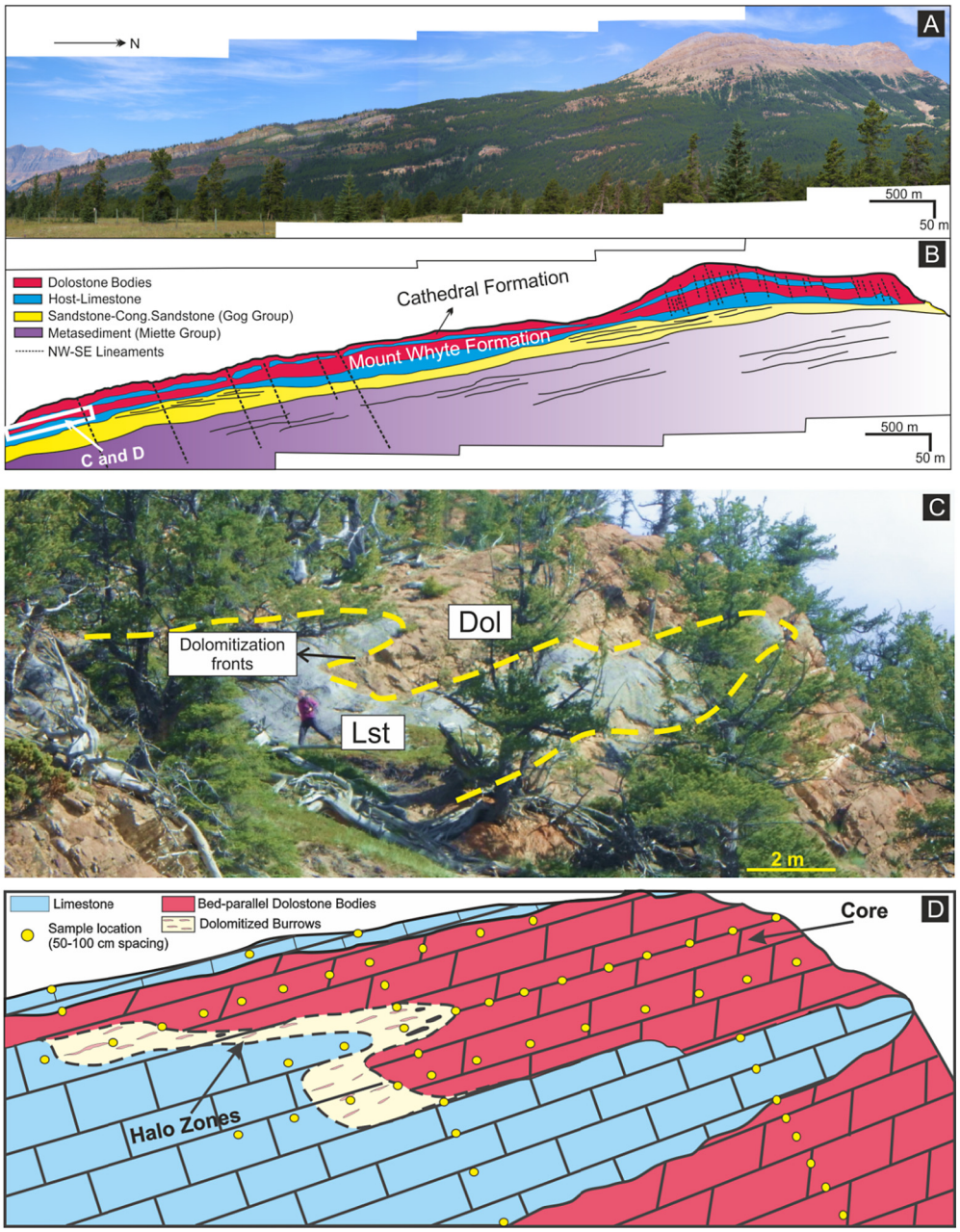

Fig. 2. (A-B). Overview of the outcrop in the Whirlpool Point locality, it shows km-scale non-stratabound bodies with stratabound terminations for both the Mount Whyte Formation and Cathedral Formation. (C-D). Termination of dolomite bodies (brown) into the limestone (gray), showing a scalloped-shaped front. Here, we collected high-resolution (50-100 cm) sampling from different sub-horizontal and vertical transects.

the thrust sheets and show a wide range of dimensions from m- to km-wide and up to 35 m thick (Fig. 2A-B).

2.2. Dolomitization

This study is part of a wider investigation of the source of fluids and magnesium for dolomitization of the Mount Whyte Formation and Cathedral Formation and focuses specifically on the genesis of the dolomite-limestone contact. Previous studies have highlighted the importance of multiphase dolomitization in the formation of HTD bodies in the Cambrian, Western Canada (e.g. Davies and Smith, 2006; Powell et al., 2006). The dolomitizing fluids are interpreted to be sourced from mixing of Cambrian seawater with hot, highly saline crustal brines driven along syn-depositional normal faults in the Cambrian (Koeshidayatullah et al., 2020).

3. Methodology

High-resolution sampling (50-100 cm spacing) was conducted on three sub-horizontal and two vertical transects (7-10 m in length) across the dolomite body (core to margin), halo zones (partially replaced limestone) and adjacent limestone in the Mount Whyte Formation at Whirlpool Point (Fig. 2C-D). Petrographic and cathodoluminescence analyses were performed on forty-two samples using a CITL cold cathode optical cathodoluminescence system mounted on a Nikon microscope eclipse CiPOL at the University of Manchester. Thin section porosity analysis (i.e. visible porosity from the blue-dyed thin section images) was conducted by using jPOR^{TM} for ImageJ (Grove and Jerram, 2011). Four to five images for each thin section were analyzed to verify the values are statistically representative (accuracy: ±0.5%). This analysis provides a minimum total porosity in the sample. Quantitative mineral map-

ping (QEMSCAN™) (following a method proposed by Amao et al., 2016) was performed to quantify mineral components and porosity, and Electron Probe Microanalysis (EPMA) was conducted to analyze dolomite stoichiometry.

Fluid inclusion micro-thermometric measurements were performed on doubly polished thick sections that were prepared using techniques designed to avoid extensive heating of samples (Goldstein and Reynolds, 1994). Measurements were made using both LINKHAM THMSG 600 and LINKAMMDSG-600 heating and cooling stage at the University of Alberta and University of Manchester, respectively. Errors of homogenization (Th) and last ice melting (Tm) temperatures were ±1.0 °C and ±0.3 °C, respectively based on analysis of synthetic fluid inclusions (Shelton and Orville, 1980). Inclusions analyzed in this study were aqueous, two-phase, primary inclusions (classification of Roedder, 1984).

Geochemical sampling (X-ray Diffraction (XRD), trace elements, $\delta^{13}C$ and $\delta^{18}O$, and clumped isotopes (Δ_{47}) analyses were conducted on thin section billets that were sampled using a microdrill assembly under a binocular microscope to extract different dolomite and limestone phases. A Bruker D8Advance Diffractometer at the University of Manchester was utilized to semi-quantitatively determine the bulk mineralogy of all dolomite and limestone samples. The XRD data were refined with the Rietveld program Topas 4.1. Dolomite stoichiometry (mol% $MgCO_3$) was calculated from the XRD pattern following the method of Lumsden (1979) while the degree of dolomite ordering was semi-quantitatively determined using the ratio between $d_{(015)}$: $d_{(110)}$ reflection peaks (Kaczmarek and Sibley, 2014).

A total of 10 samples were analyzed for their iron concentration by using Perkin-Elmer Optima 5300 dual view Inductively Coupled Plasma Atomic Emission Spectroscopy (ICP-AES) at the University of Manchester. The sample extraction procedure was using a standard carbonate digestion process where 6M hydrochloric acid (HCl) and 10 mL de-ionized water were added to ensure that total dissolved solids will be less than 0.1%. The produced liquids were filtered to remove particles >0.45 µm and acidified by using 2% HNO_3. Detection limits for both analyses are as low as 0.01 ppb in solution under the usual operating conditions with reproducibility of ±5% (1σ).

Stable isotope analysis ($\delta^{18}O$ and $\delta^{13}C$) was performed on 35 samples (5-10 mg) that were reacted with H_3PO_4 for 16 h at 25 °C for calcite, and 48 h at 50 °C for dolomite. The samples were analyzed at the Scottish Environmental University Research Centre (SUERC) and University of Liverpool, UK by using a VG OPTIMA and VG SIRA 12 gas-source mass spectrometer, respectively. A fractionation factor of 1.01025 (Kim and O'Neil, 1997) was applied to the $\delta^{18}O$ values to correct for carbonate-phosphoric acid digestion for calcite and similarly for dolomite by using fractionation of 1.01066 (Rosenbaum and Sheppard, 1986). All values are reported as delta values with respect to the Vienna PeeDee Belemnite (VPDB) and standardized to marble and NBS-19. Average analytical precision (1σ) and reproducibility for both calcite and dolomite was checked by replicate analysis and it is better than ±0.1‰.

Δ_{47} analyses were performed on eleven dolomite and four limestone samples by using Dual inlet Thermo Scientific 253 and 253+ ultra-high-resolution isotope ratio mass spectrometers at the Stable Isotope Laboratory, University of Miami. The CO_2 extraction procedures and measurements followed the description of Staudigel et al. (2018). Three replicate measurements were performed to check for consistency and correct for the error and/or drift over time. The results were reported by using the absolute reference frame as suggested by Dennis et al. (2011) (Carbon Dioxide Equilibrated Scale (CDES)). Conversion from Δ_{47} value to temperature was following the equation of Staudigel et al. (2018) modified for dissolution at 90 °C and without applying acid fractionation factor. In addition, during the measurement of clumped isotopes, $\delta^{13}C$ and $\delta^{18}O$ values were also measured. As the reaction was conducted at 90 °C, the $\delta^{18}O_{dolomite}$ values were constantly corrected by 1.0008 to account for the differential fractionation of CO_2 yielded from dolomite relative to calcite (Sharma and Clayton, 1965). The calculation of $\delta^{18}O_{water}$ of parent fluid was determined by using the Δ_{47} temperatures and the published oxygen fractionations of calcite-water (Kim and O'Neil, 1997) and dolomite-water (Horita, 2014).

4. Results

4.1. Geometry of dolomite bodies and dolomitization fronts

In the study location, the Mount Whyte Formation is mainly composed of mudrock, bioturbated mudstone and oncoidal grainstone (~80 m thick). The HTD dolomite bodies typically occur as bed-parallel and –perpendicular massive bodies with multiple vertical and lateral termination points. The dolomite bodies are readily identified in outcrop by their contrasting orange-brown (dolomite) and gray (limestone) (Fig. 3A). The bed-parallel dolomite bodies and terminations occur within burrowed mudstone facies and are over- and underlain by undolomitized oncoidal grainstone and mudrock at the top and base, respectively (Fig. 3A-B). In contrast, bed-perpendicular bodies occur at a much smaller scale (decimeter scale, up to 1 meter wide) and in proximity to NW-SE trending fracture or fault zones (Fig. 3C).

Dolomitization fronts occur at the top and base of the dolomite bodies (herein referred to as 'vertical contacts') and within beds (referred to as 'lateral contacts'). Well-preserved lateral contacts represent fronts that formed within apparently homogenous layers that show no apparent change in physical rock properties at or near the termination of the dolomite body. This type of contact is commonly observed in the Mount Whyte Formation, and has several different geometries, which can principally be described as scalloped- and finger-like (Fig. 2C and 3D). These lateral contacts can be recognized at various scales, from a few centimeters to tens of meters and are perpendicular to the bedding strike. Terminations are typically diffuse and nonplanar, with a wide halo zone (up to 1 m), defined as a zone of partially replaced limestone (Figs. 2C and 3D). In outcrop, this halo zone is defined by a mottled color contrast between dolomitized burrows and limestone. In thin section, the contact between the burrows and the limestone is sharp (Fig. 4B and E). In contrast, vertical contacts are usually sharp and planar and can be either be parallel or perpendicular to the strike of the bedding with no, or very thin, halo zones (Fig. 3B and D).

4.2. Micro- to macro-scale rock and mineral properties

Limestone—Laterally adjacent to the dolomite bodies (i.e. within the same bed), the limestone comprises homogenous, fine-grained micrite (Fig. 4A). In contrast, the limestone directly overlying the dolomite is predominantly composed of oncoidal grainstone that has been pervasively cemented by blocky marine cement (Fig. 4B). Both the mudstone and the cemented oncoidal grainstone facies have a low average porosity, 0.9% and 1.6%, respectively; (Table 1).

Halos and Dolomitization Fronts—Within the halo zones, the limestone is partially dolomitized with two dolomite textures: 1) finely crystalline (30-150 µm), euhedral dolomite, poorly ordered and magnesium-poor (av. 0.62 and 47.6 mol% $MgCO_3$) (Figs. 4C-D, 5A and Table 1) and 2) coarse (250-1000 µm), non-stoichiometric, poorly ordered saddle dolomite (av. 46.2 mol% $MgCO_3$ and 0.64) (Fig. 4E-F and Table 1). QEMSCAN™ analysis reveals the presence of authigenic, pore-filling quartz associated with these dolomite

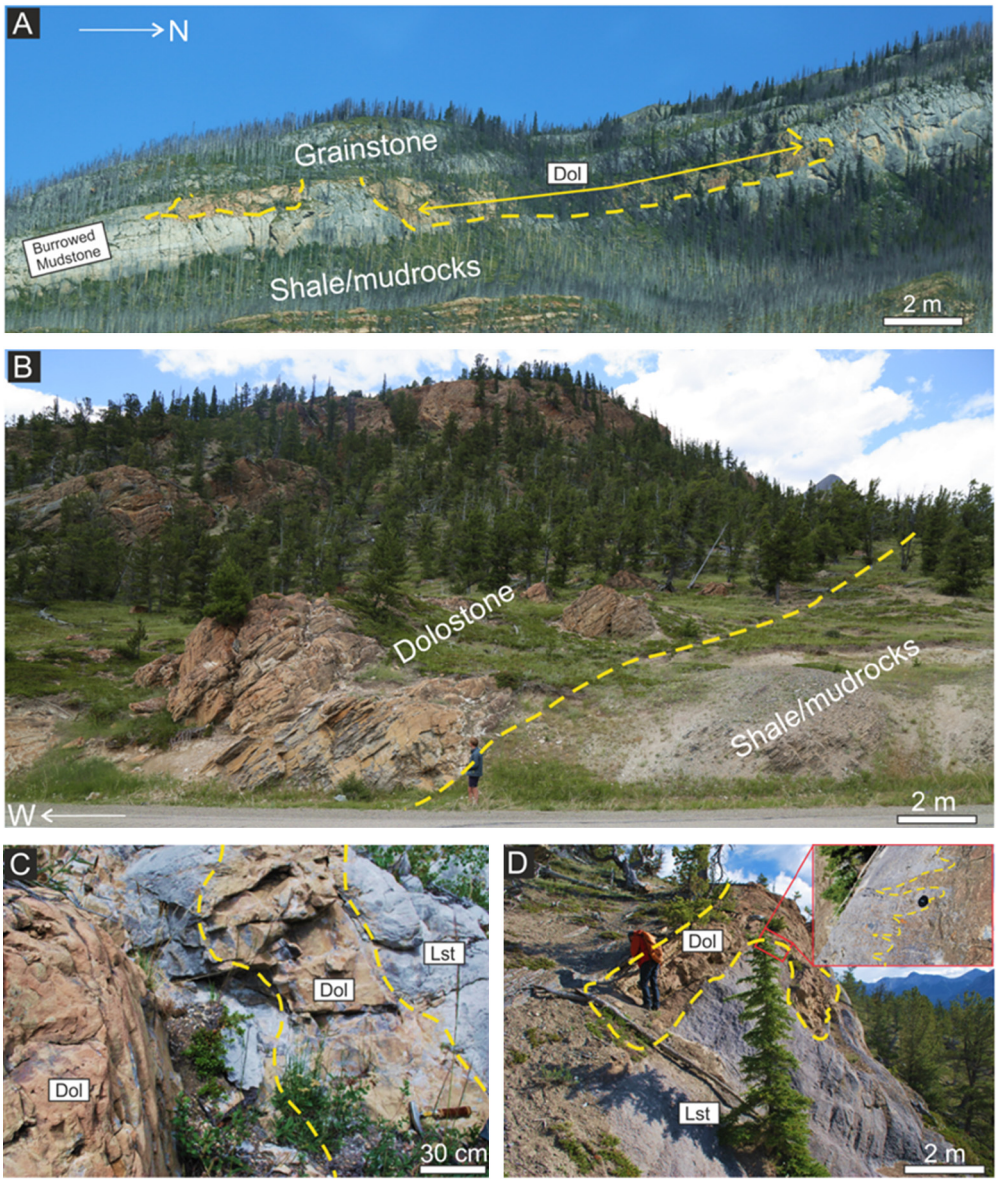

Fig. 3. Variations in HTD dolomite bodies and dolomitization fronts geometries observed in the Mount Whyte Formation. (A). Bed-parallel dolomite bodies with tongue-shaped fronts as the lateral contact. (B). Vertical bed parallel contact between dolomite body and undolomitized, mudrock with a sharp boundary. (C). Small scale bed-perpendicular bodies with sharp and nonplanar lateral dolomitization fronts. (D). Bed-parallel body with a sharp vertical contact with the overlying undolomitized, well-cemented grainstone bed and a lateral transition, bed-perpendicular transition to bioturbated mudrocks.

crystals (Fig. 4G). Overall, the halo zones show high interparticle porosity (up to 11.6%. av. 7.5%; Table 1) (Fig. 4H).

Proximal and inboard of dolomite-limestone contacts, the replacement dolomite is fabric-destructive and characterized by euhedral to subhedral dolomite crystals with cloudy cores and clear crystal rims and a unimodal crystal size distribution (50-150 µm). The euhedral dolomite displays a red to purple core with single to multiple, thin to thick bright orange cathodoluminescent zones at the rims (Fig. 5B and D). XRD analysis shows it to be non-stoichiometric (av. 47.6 mol% $MgCO_3$) and poorly ordered (av. 0.62). In situ electron probe microanalysis of this euhedral dolomite also further confirm the occurrence of non-stoichiometric dolomite mineral near the dolomitization front (av. 46.2 mol% $MgCO_3$) (Table 1). Intercrystalline porosity often occurs within this texture; digital image analysis determined porosity ranges from 3.6% to 8.5% (av. 5.6%; Supplementary material).

Main Dolomite Bodies—Samples were collected across the main dolomite bodies, inboard of the reaction front for about 15 m, with the most distal samples from the dolomite – limestone margin referred to as the 'core' (Fig. 2D). These samples mainly exhibit a similar, fabric destructive texture with subhedral to anhedral dolomite crystals (Fig. 5E and G) with bimodal sizes (60 to 480 µm) (Fig. 5E and G). This type of dolomite is stoichiometric (av. 50.2 mol% MgCO3), relatively well-ordered (av. 0.89) and shows interlocking, mosaic crystals with very low average porosity (av. 1.5%; Table 1). In thin section, subhedral and anhedral dolomites nucleate on and replace the euhedral dolomite (Fig. 5E). The replacive subhedral to anhedral dolomite have a dark red luminescent core and weak, brighter orange outer zones (Fig. 5F). In some cases, there is an overgrowth of pore filling, dull-bright zoned of nonplanar dolomite cement that occludes porosity (Fig. 5H). Overall, the bright orange zone becomes narrower and the luminescence is duller at the core of the dolomite bodies, compared to the margin of the bodies. Overall, the dolomite is more stoichiometric, cation ordering higher and porosity lower in the core of the

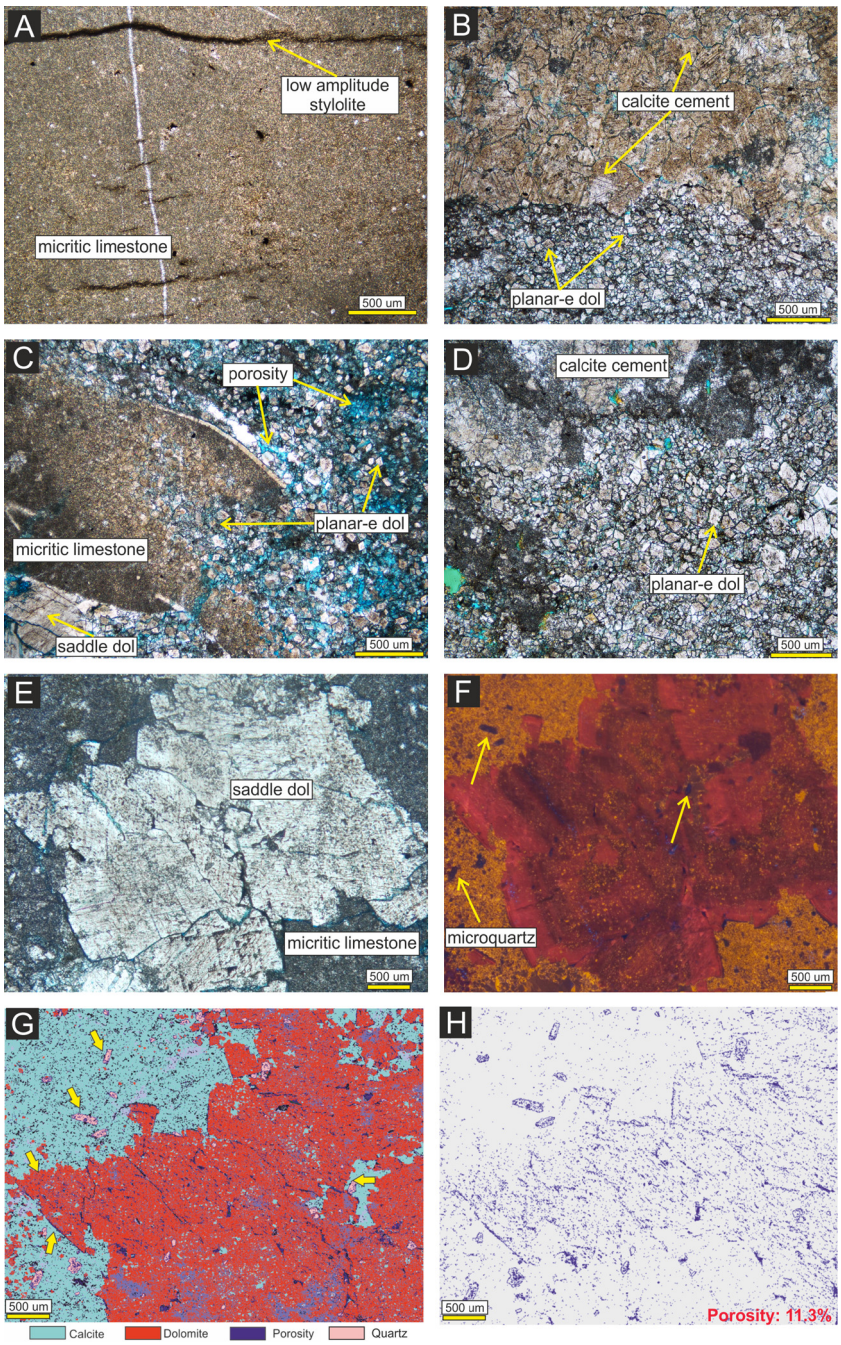

Fig. 4. Thin section of limestones and different dolomite fabrics in the halo zones. (A). Micrite-dominated limestone collected adjacent laterally to the dolomite bodies. (B). Sharp contact between euhedral dolomite and well-cemented grainstone. (C-D). Partially replaced of micritic limestones by euhedral-subhedral dolomites. This fabric is typical in the halo zones. (E). The presence of coarse, saddle dolomite texture in the halo zones. (F). Cathodoluminescence characteristic of (E) showing compositionally zoned luminescence. (G-F). QEMSCAN image of (E) that confirms the mineralogical identification from thin section. In addition, it exhibits the presence of authigenic, hexagonal quartz and abundance interparticle-intraparticle porosities.

dolomite bodies compared to the dolomitization fronts and halo zones (Fig. 6A-B; Table 1).

4.3. Geochemistry

The geochemical results are described for the three different elements of the dolomite – limestone transition.

Limestone—Stable isotope values ($\delta^{18}O_{calcite}$ and $\delta^{13}C_{calcite}$) values of the limestone adjacent to the dolomite bodies display a narrow range, (-10.6 ± 1.2‰ and -0.7 ± 0.2‰ VPDB, respectively; Table 1), as do the Δ_{47} values (0.365 ± 0.013‰). This gives a calculated temperature of 164 ± 15.7 °C and $\delta^{18}O_{water} = +10.7 \pm 2.1$‰ SMOW from Δ_{47} values (Table 1). The range of Fe concentrations in the limestones is between 1360-1623 ppm.

Halos and Dolomitization Fronts—While the $\delta^{13}C_{dolomite}$ in this zone are comparable to the limestone (av. -0.3 ± 0.4‰), the $\delta^{18}O_{dolomite}$ values are lighter (av. -15.8 ± 0.7‰). Fluid inclusion analysis obtained homogenization temperature (Th) values ranging from 121 ± 25.3 °C (Table 1). The Δ_{47} temperatures are also show a wide range values, 136 ± 21 °C, depending on the sample location (i.e. cooler towards the upper section). Overall the Δ_{47} temperatures are higher than Th even after the pressure correction was applied to Th (see Koeshidayatullah et al., 2020 and supplementary material). Honlet et al. (2018) have observed similar relationship

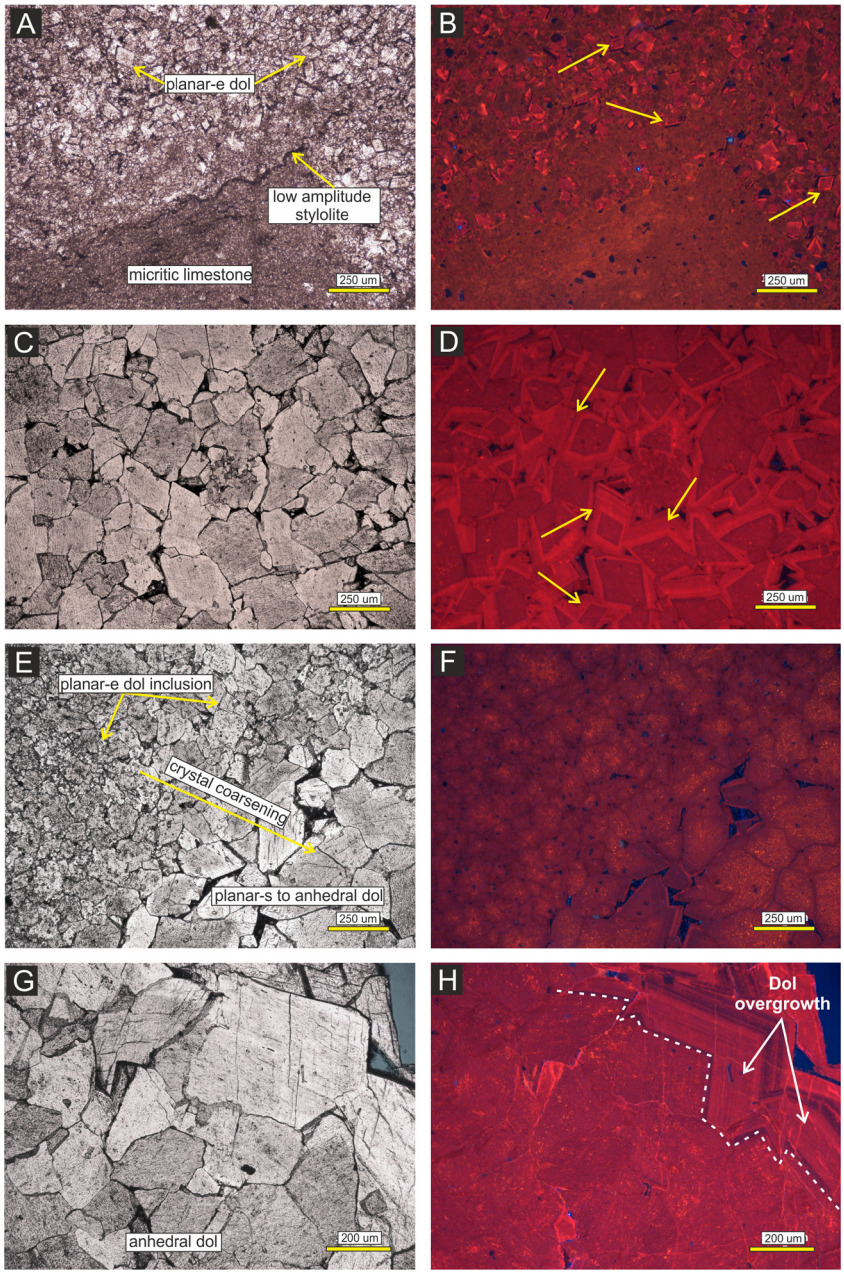

Fig. 5. Thin section images of different dolomite fabrics observed in the margin and core of dolomite bodies. (A). Euhedral dolomite fabric partially replacing micritic limestone. (B). Cathodoluminescence image of (A) displaying thin bright rim orange luminescence. (C). A typical of euhedral fabric showing cloudy core and clear rim, but with coarser crystal size. (D). Cathodoluminescence image of (C) displaying compositionally zoned luminescence. (E). Thin section image showing two different dolomite fabrics, euhedral and anhedral. (F). Cathodoluminescence image of (F) displaying no to very weak luminescence zonation. (G). Subhedral to anhedral dolomite fabrics replaced/recrystallized the euhedral dolomite. (H). Cathodoluminescence image of (G) displaying the presence of thick luminescence zonation. This zonation represents dolomite overgrowth that filling the pore space.

and suggested that the difference is controlled by the crystallization pressure and also the Δ_{47} may represent the actual entrapment/crystallization temperature while the Th represents the minimum crystallization temperature. The calculated $\delta^{18}O_{water}$ of the dolomite fabrics in this zone are -0.6 ± 2.8‰ SMOW. Unlike the limestone, the dolomites observed within the dolomitization fronts and halo zones, are significantly enriched (almost six times) in Fe compared to the limestone (8225 ± 1021 ppm).

Main Dolomite Bodies—The $\delta^{18}O_{dolomite}$ and $\delta^{13}C_{dolomite}$ values of dolomites in the main zone are similar to the dolomitization fronts and halo zones, being -15.6 ± 0.6‰ and -0.5 ± 0.4‰, respectively. Here, the dolomites exhibit two populations of both Th and Δ_{47} temperatures depending on their distance from the margin of dolomite bodies, with an overall increase in temperature from the margin towards the core of the bodies (Fig. 7). In the middle section of the main bodies, the values of Th and Δ_{47} show a 20-40 °C difference, 147 ± 28 °C and 164 ± 16.4 °C, respectively. In the core of the body, the temperature difference between Th values and Δ_{47} is slightly higher; 181 ± 23.6 °C for Th and 206 ± 19.2 °C for Δ_{47} (Table 1). Conversely, these dolomites display a narrow range of $\delta^{18}O_{water}$, calculated in the middle and core sections as $+2.3 \pm 1.3$ and $+5.4 \pm 1.1$‰ SMOW, respectively. Regardless of the difference in their texture and geochemical signals, the dolomite crystals in this zone have a high Fe concentration compared to dolomite in the dolomitization fronts and halos (8344 ± 329 ppm

Table 1
Results from dolomite micro-and macro-properties, and geochemistry analyses from the three studied transect.

Phase	Dolomite stoichiometry (mol% MgCO3) (XRD)	Dolomite stoichiometry (mol% MgCO3) (EPMA)	Cation ordering (015/110)	Fe (ppm)	Thin section porosity (%)	$^{13}C_{VPDB}$ (‰)	$^{18}O_{VPDB}$ (‰)	Δ47-RF (CDES @ 90 °C)	$T\Delta_{47}$ (°C)	Th (°C)	$^{18}O_{water}$ (SMOW)
Limestone (Transect 1-3)											
Min	–	–	–	1360	0.2	−0.9	−11.7	0.324 ± 0.001	142	–	8.2
Max	–	–	–	1623	3.2	−0.3	−8.9	0.385 ± 0.023	214	–	14.7
Mean	–	–	–	1510	1.3	−0.7	−10.6	0.365 ± 0.013	164	–	10.7
SD	–	–	–	108	0.8	0.2	1.2	–	20.4	–	2.1
Dolomite-Limestone Contact and Halos (Transect 1-3)											
Min	45.4	44.7	0.55	6920	3.3	−0.8	−16.7	0.366 ± 0.018	93	91	−6.0
Max	50.5	51.2	0.78	9419	11.6	0.1	−15.1	0.452 ± 0.025	162	153	2.2
Mean	47.6	46.2	0.62	8225	7.5	−0.3	−15.8	0.395 ± 0.026	136	124	−0.6
SD	1.2	2.8	0.10	1021	2.6	0.4	0.7	–	21	25.3	2.8
Main Dolomite Body (Middle) (Transect 1-3)											
Min	48.5	–	0.77	7723	0.5	−0.8	−16.4	0.345 ± 0.008	130	121	−0.3
Max	52.7	–	1.00	8478	3.0	−0.4	−15.1	0.400 ± 0.018	185	189	4.1
Mean	49.4	–	0.82	8344	1.5	−0.6	−15.6	0.365 ± 0.012	164	147	2.3
SD	1.3	–	0.1	329	0.7	0.2	0.5	–	16.4	28.0	1.3
Main Dolomite Body (Core) (Transect 1-3)											
Min	48.8	48.1	0.81	6928	0.2	−0.9	−16.7	0.308 ± 0.007	174	161	3.5
Max	51.1	51.1	1.00	9352	3.4	0.3	−14.9	0.354 ± 0.016	239	218	7.0
Mean	50.2	49.3	0.89	8553	1.4	−0.4	−15.5	0.330 ± 0.010	206	181	5.4
SD	1.0	1.2	0.08	1577	0.8	0.5	0.7	–	19.2	23.6	1.1

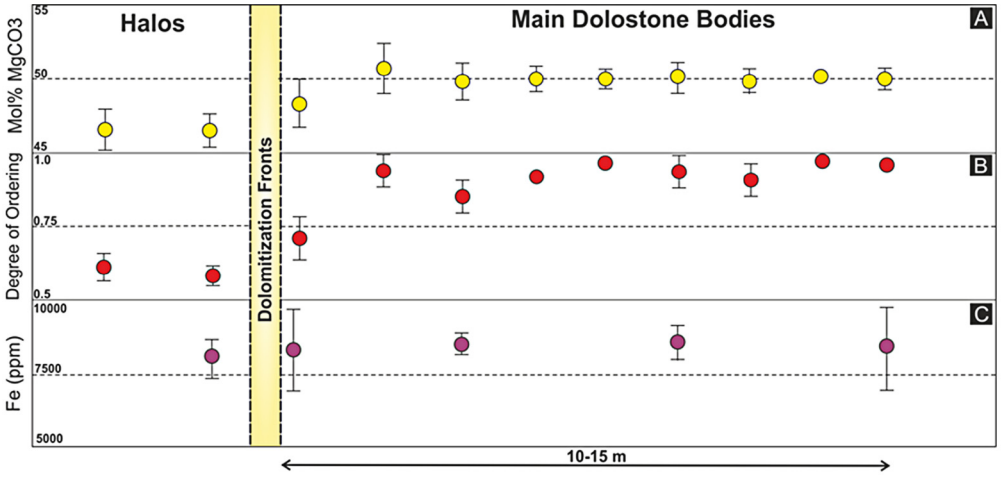

Fig. 6. Lateral profiles of dolomite stoichiometry, cation ordering and Fe concentration collected from the three transects across dolomite bodies and dolomitization fronts. (A). Dolomite stoichiometry showing a systematic pattern of depletion in magnesium content towards the dolomitization fronts and halo zones. (B). Similar depletion of cation ordering of dolomite towards the margin of dolomite bodies. (C). Fe contents across the dolomite bodies showing invariant values.

in the middle section and 8553 ± 1577 ppm in the core; Table 1 and Fig. 6C).

5. Discussion

5.1. Controls on the formation of HTD dolomitization fronts

The origin of dolomitization fronts in hydrothermal dolomite bodies has only been described in detail by a few studies (Wilson et al., 1990; Nader et al., 2007; Merino and Canals, 2011). Where dolomitization fronts occur against specific structural features (e.g. fractures, stylolites) or facies boundaries, then it is reasonable to assume that dolomitization terminated as a result of a change in rock permeability (e.g. Martín-Martín et al., 2015). However, many examples of dolomitization fronts occur where no such permeability barriers are present (Nader et al., 2007; Sharp et al., 2010; Hirani et al., 2018; Koeshidayatullah et al., 2020). In these cases, the termination of dolomite bodies must be governed by a reduction in dolomitization potential, related to: (i) changes in the supply of diagenetic fluids associated with a cessation of tectonic activity or uplift that can either close the fluid pathways (e.g. fault) or change the hydrological regimes (e.g. Morrow, 1982; Machel, 2004), (ii) cooling of dolomitizing fluids (e.g. Wilson et al., 1990; Davies and Smith, 2006), or (iii) a decrease in the Mg/Ca ratio of the dolomitizing fluid (Wilson et al., 1990).

The proximity of dolomite bodies in this study to NW-SE trending faults and fractures suggests that fluids were supplied along faults, during co-seismic dilatancy events, which along with high heat flow facilitated dolomitization in this formation (Koeshidayatullah et al., 2020). Such a process is thought to have persisted until the late Cambrian (Powell et al., 2006; Davies and Smith, 2006), evidenced by the pervasive, multiphase high temperature dolomitization of the overlying Cathedral Formation and Eldon Formation (e.g. Davies and Smith, 2006 and reference therein). This suggests that dolomitization was a long-lived process and that supply of dolomitizing fluids to the Cambrian succession in the study area was maintained for several million years (5-10 m.y).

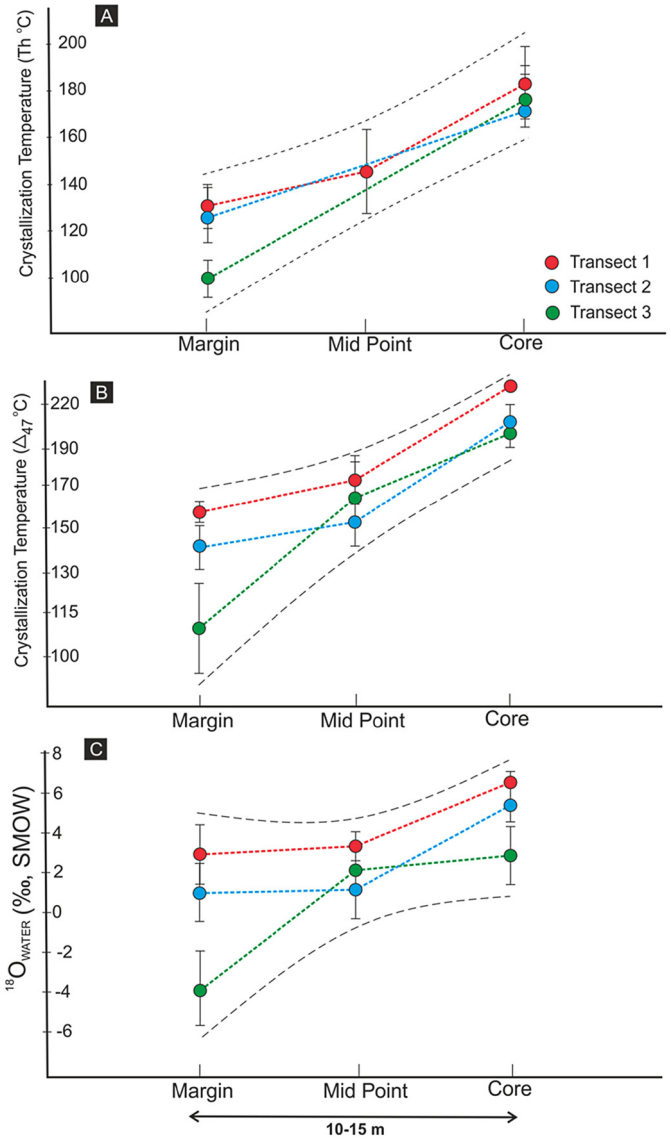

Fig. 7. Profiles of temperature and $^{18}O_{water}$ across dolomite bodies analyzed from three different sub-horizontal transects. (A). Temperature profile from fluid inclusion analysis. (B). Temperature profile from clumped isotope analysis. (C) $^{18}O_{water}$ profile calculated by using ^{18}O-water fractionation (Horita, 2014) and clumped isotope temperature.

Clumped isotope and fluid inclusion data show a consistent profile of increasing temperature from the margin of dolomite bodies towards the core (Fig. 7A-B). Temperature-controlled termination of dolomitization has been proposed by previous studies (e.g. Wilson et al., 1990), as dolomitization is kinetically favored and more efficient at higher temperatures. However, even on the margin of the dolomite bodies in this study, the temperature of dolomitization (av. 206 °C to av. 132 °C) is well above the temperature that is conducive for dolomitization (≥50 °C; Machel, 2004). Consequently, although the cooling of dolomitizing fluids would have had an impact on the concentration and ionic strength of Mg in the fluids (e.g. Morrow, 1982; Wilson et al., 1990; Kaczmarek and Thornton, 2017), temperature alone may not be enough to explain the formation of dolomitization fronts in this case.

If the Mg/Ca ratio of a dolomitizing fluid is lowered, as expected to occur during dolomitization, its dolomitization potential will be lowered and dolomitization can terminate (Merino and Canals, 2011). At the dolomite-limestone contact, and within the halo zones, euhedral and subhedral dolomite is less stoichiometric (i.e. $<_{0.5}$Mg) and less well ordered than the core of the dolomite bodies (Fig. 6A). This could be explained in several ways:

(i) Decreasing stoichiometry as a result of an increase in Fe concentration. Lumsden et al. (1995) and Gregg et al. (2015) showed that incorporation of Fe^{2+} into the dolomite lattice may increase reaction rates and decrease dolomite stoichiometry. In this study, however, high Fe concentrations (~8500 ppm) are found in both non-stoichiometric, poorly ordered dolomite at the limestone-dolomite contact and stoichiometric, well-ordered dolomite within the main bodies. This suggests that Fe concentration does not affect the distinct variation in dolomite stoichiometry and ordering observed in this study.

(ii) A temperature control on dolomite stoichiometry. Kaczmarek and Thornton (2017) and Kaczmarek et al. (2017) showed a linear relationship between temperature and dolomite stoichiometry across a temperature gradient of 160 to 250 °C, although the precipitated dolomite remained non-stoichiometric (max. 46 mol% $MgCO_3$) until primary recrystallization took place. Results from our study are slightly different, with a systematic decrease in temperature from the core (av. 206 °C) to middle (av. 164 °C) to the dolomitization front (av. 136 °C) (Fig. 7A-B). In tandem, stoichiometry remains similar in the core of the dolomite body, decreasing suddenly at the transition from the anhedral-saddle dolomite in the main body to euhedral – subhedral dolomite in the dolomitization fronts and halos (Fig. 5E). This would suggest that temperature variations alone couldn't explain the systematic changes in dolomite stoichiometry observed in this study.

(iii) Calcitization of the dolomite or a decrease in fluid Mg/Ca ratio. The poor stoichiometry of the dolomite within the halo and dolomitization front could be related to calcitization of the dolomite, but this was not observed in thin section, by staining, or by QEMSCAN™ analyses. This would suggest that the calcium enrichment of the dolomites is a primary feature, related to the dolomitization process and potentially the Mg/Ca ratio in the fluids. A similar depletion in Mg/Ca ratio at dolomite - limestone contacts was observed by Nader et al. (2007). The depletion in the Mg/Ca ratio of the dolomitizing fluid could occur as the result of progressive dolomite precipitation, as it migrated away from the fluid source. Merino and Canals (2011) proposed that a sudden decrease in Mg concentration would occur at the head of an advancing dolomitizing fluid as Ca^{2+} is released during rapid dolomitization, creating coarsely crystalline, non-stoichiometric dolomite. Hence, the abrupt changes in stoichiometry within the Mount Whyte Formation may be explained by such a self-accelerating process (Fig. 4E). However, the importance of fluid cooling in terminating dolomitization cannot be completely ruled out.

5.2. Evolution of fluid flow and dolomitization fronts

5.2.1. Multistage fluid flow

The formation of large-scale HTD dolomite bodies is often interpreted to involve multiple stages of dolomitization (e.g. Davies and Smith, 2006; Sharp et al., 2010; Hollis et al., 2017). Deciphering the paragenesis of such multistage dolomitization requires observation of (i) crosscutting relationships of different dolomite fabrics or bodies, and (ii) different elemental or isotopic signals of the different dolomitization stages (e.g. Machel, 2004). Nevertheless, in many field examples including this study, petrographic observation showed no distinct crosscutting relationships between the different fabric of replacive dolomites and their geochemical signals (i.e. Fe and Mn concentrations, $\delta^{18}O_{dolomite}$) are also very similar. It can

therefore be almost impossible to unravel the fingerprint of multiple phases of dolomitization within a single dolomite body.

Instead, this study utilizes the variations in $\delta^{18}O_{water}$ and crystallization temperature across the dolomite bodies (Fig. 7A-C) to unravel the origin of multiphase dolomitization in the Mount Whyte Formation. The increase in temperature and $\delta^{18}O_{water}$ from the margin to the core of the dolomite body, suggesting fluids became more evolved and hotter during subsequent phases of dolomitization (Fig. 7C). This temperature difference between the margin and core of dolomite bodies, over a short distance ($<$15 m) corroborates the idea that multiple pulses of fluid occurred within single dolomite bodies. This is also consistent with the change in dolomite textures and stoichiometry. Kaczmarek and Sibley (2014) and Kaczmarek and Thornton (2017) show the formation of dolomite crystals involves several replacement-recrystallization processes through different time steps from non-stoichiometric to stoichiometric dolomite until they become 'stable' (i.e. no more changes in stoichiometry) by uninterrupted fluid flux. In natural settings, uninterrupted fluid flux would require a continuous supply of fluids or numerous, discrete pulses of fluid migration.

5.2.2. "Retreating" dolomitization fronts

As well as being less stoichiometric and less ordered, the dolomite crystals at the dolomite-limestone contacts and within the halo zones are more compositionally zoned (Fig. 5A-F), than at the core of the dolomite bodies (Fig. 6A-B). Furthermore, the dolomitization fronts and halo zones have a cooler temperature and are more porous than the main dolomite bodies (Figs. 5 and 7A-B). This phenomenon could occur if the reaction front is (i) the youngest part of the dolomite body where the fronts act as the latest residue of the dolomitization process, or (ii) it is older than the core of the dolomite body but has not undergone recrystallization because subsequent flux of dolomitizing brine did not permeate as far as this contact.

In the first scenario, the dolomite body is interpreted to have become wider with each subsequent flux of dolomitizing brines. This requires that fluids continued to migrate and react to greater distances from the fluid source with each subsequent flux of fluid. For this, the dolomite must remain permeable. Reactive transport models show that this can occur with constant fluid flow, such that dolomite bodies extend further away from the fluid source through time (Corbella et al., 2014). Some outcrop studies have also interpreted the evolution of dolomitization fronts to occur by the progressive, lateral, forward movement of fronts through time, away from the fluid source (e.g. Wendte, 2006; Merino and Banerjee, 2008). Numerical simulations indicate, however, that such a model of a forward-propagating reaction front requires that the dolomite body remain porous and permeable throughout the replacement process (e.g. Merino and Canals, 2011; Corbella et al., 2014). Although most reactive transport models take into account porosity-permeability feedback through mineral replacement processes, they do not always simulate overdolomitization, which is often seen in natural systems (e.g. Saller and Henderson, 1998). Recently, Yapparova et al. (2017) simulated progressive porosity loss during HTD dolomitization in proximity to a fault that sourced dolomitizing fluids. This is consistent with what is observed in this study and other outcrop studies on HTD dolomitization (Wilson et al., 2007; Sharp et al., 2010; Hirani et al., 2018) where the highest porosity is preserved towards the margins of the dolomite body and their adjacent halos. Such an outcome could be achieved by scenario 2, whereby the features observed in the dolomitization fronts in the Mount Whyte Formation are older than the core of the dolomite bodies. In this scenario, subsequent pulses of the dolomitizing fluids did not reach the position of the first dolomitization front, and thereby the dolomite – limestone contact and the halo preserve the original features of the earliest phase of dolomitization. This could have occurred if, during the initial replacement phase, the dolomitization front advanced through a dissolution-reprecipitation process that generated porosity (e.g. Putnis, 2009; Kondratiuk et al., 2015) until there was a decrease in the dolomitizing potential of the fluid and the reaction terminated (Fig. 8). Subsequent phases of fluid flux then recrystallized the precursor dolomite, and crystal size increased to create an interlocking crystal texture, as has been shown to occur experimentally by Kaczmarek and Sibley (2014) and Kaczmarek et al. (2017). Pore volumes and permeability were thereby reduced, and subsequent phases of dolomitizing fluids could not advance so far from the fluid source (Fig. 8).

This process can also explain the variations in dolomite textures and cathodoluminescence zonation observed between the halos, margin and core of the bodies in the Mount Whyte Formation. Olanipekun and Azmy (2017) reported recrystallization of early, non-stoichiometric zoned dolomite to well-ordered, stoichiometric and nonplanar, unzoned dolomite crystals in a drive towards equilibrium and lower free energy. It is therefore feasible that the zoned crystals observed at the dolomitization front and in the halo reflect fluid-compositional gradients that were created during the earliest phase of dolomitization. Subsequent recrystallization of most of the dolomite body would then have led to equilibration and growth of unzoned dolomite crystals (Figs. 6E-G and 8).

Based on this model, the cooler temperatures recorded at the dolomitization fronts record the oldest, most laterally extensive phase of dolomitization in the Mount Whyte Formation. Subsequent phases of fluid flux were hotter, but did not advance so far. Instead, recrystallization of older phases of dolomite created less zoned, more stoichiometric and well ordered, interlocking crystal mosaics, reducing porosity (Fig. 8). In this sense, the temperature gradient that is preserved is not evidence for a decrease in fluid temperature during dolomitization, but rather records recrystallization by progressively hotter fluids. It is therefore not possible to confidently determine the importance of fluid cooling in governing the termination of dolomitization. Rather, the succession provides a record of how the position of the reaction fronts 'retreated' with each subsequent replacement occurring over a zone that was narrower than the previous one (Fig. 8). The present day dolostone – limestone contact is therefore the oldest reaction front within the body, frozen in time.

Other studies corroborate this notion, observing that the paragenetically earliest replacement bodies are always wider than the later, fully replaced bodies (Nader et al., 2007; Sharp et al., 2010). Although dolomite bodies formed through a low-temperature, seepage-reflux process could have completely different reaction kinetics to hydrothermal dolomitization, they display a similar spatial porosity and recrystallization/overdolomitization relationship observed in our study (e.g. Saller and Henderson, 1998) and might also preserve a progressive retreat of reaction fronts, but temporally rather than laterally (e.g. Newport et al., 2020). Ultimately, this proposed dynamic evolution of dolomitization fronts may be applicable to the genesis and evolution of a wider range of dolomitization fronts in different dolomitization systems.

5.3. Insight to porosity enhancement around dolomitization fronts

In the Mount Whyte Formation, there is an overall trend from higher average porosity at the dolomitization front (av. 7.5%), towards a lower porosity within the main dolomite bodies (av. 1.4% to 1.5%) (Fig. 9 and Table 1). Porosity is almost entirely intercrystalline, between dolomite crystals (Figs. 4 and 5). Porosity can increase during dolomitization due to a loss in molar volume (Machel, 2004) in particular during the early stages of calcite-to-dolomite replacement due to the synchronization between rapid dissolution and slower precipitation in dolomite-saturated fluids

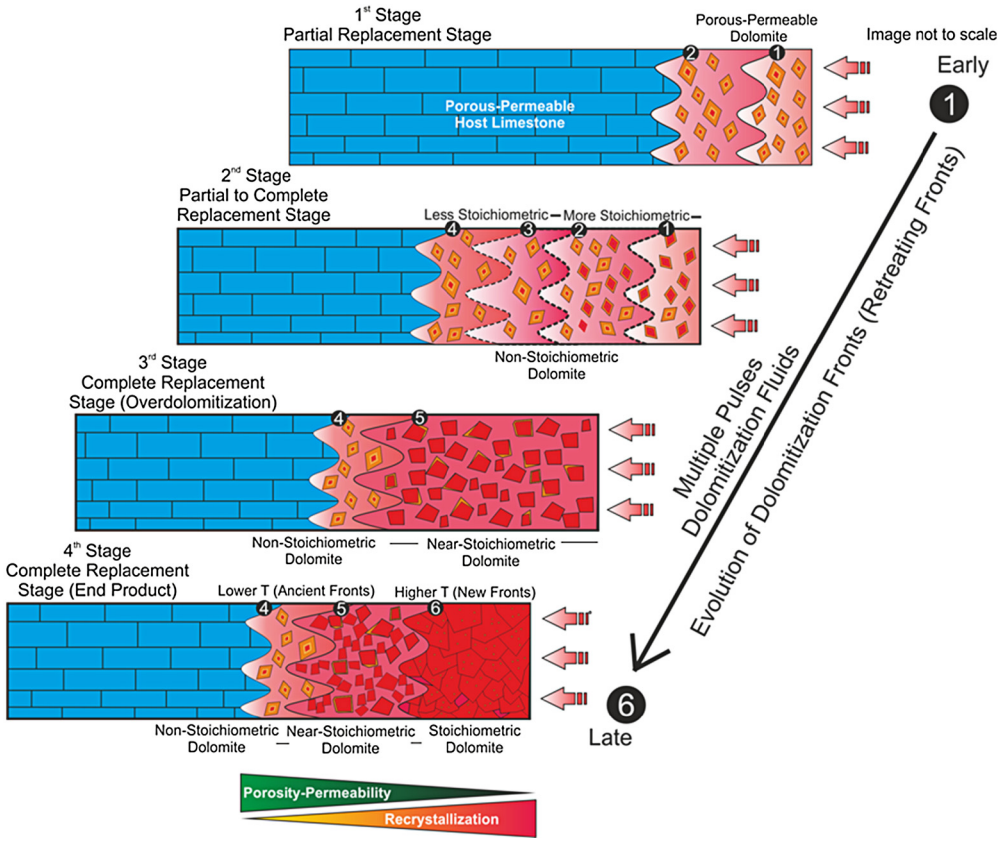

Fig. 8. A schematic diagram showing the evolution of dolomitization fronts during multiple pulses dolomitization. Note the dolomitization fronts were advancing during the partial replacement stage (stage 1-4) and evolved to retreating fronts once recrystallization/overdolomitization occurred (stage 5-6). (A-D).

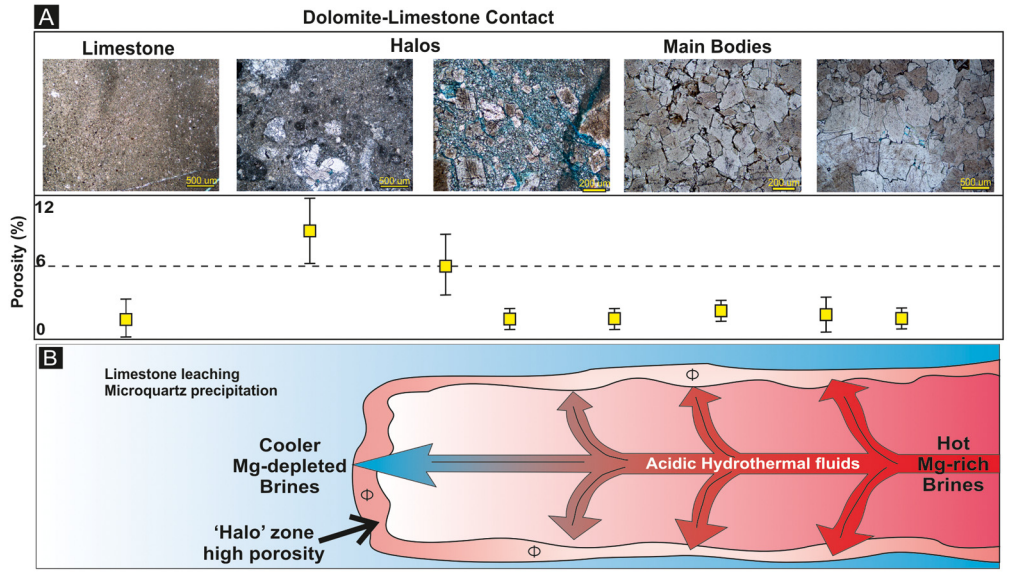

Fig. 9. Porosity profile and mode of formation in the Cambrian HTD bodies. (A). Porosity profile and the corresponding dolomite fabrics across the dolomite bodies. (B). A cartoon showing the mode of porosity formation in this study related to acidification-induced leaching.

(Putnis, 2009; Kondratiuk et al., 2015). An alternative explanation for the higher porosity at the reaction front, therefore, is that the negative volume change that occurred during the early replacement stage of dolomitization increased porosity, possibly with further porosity enhancement within the halo zones occurring by partial leaching (e.g. Wendte, 2006; Merino and Canals, 2011; Kondratiuk et al., 2015). It is not possible from the data in this study to determine how important this process was, but since the dolostone-limestone contact is interpreted to record the earliest (oldest) phase of dolomitization it is possible that porosity was generated because dolomite was precipitated more slowly than calcite was dissolved at the reaction front. Calcite solubility might also have been increased by (i) the greater solubility of calcite at lower temperatures and (ii) fluid-mixing, between latent pore water and the dolomitizing fluid (Wendte, 2006). Since, the recorded temperature near the dolomitization fronts (av. 140 °C),

are still far above the suggested temperature at which calcite solubility increases ($\lesssim$50 °C), and that temperature probably has a minor role compared to pressure and pCO_2 in determining calcite solubility (Coto et al., 2012), a temperature control on calcite solubility seems unlikely. Enhanced calcite solubility as a result of fluid mixing is possible, particularly since dolomitization is interpreted to have occurred at a relatively shallow burial depth (Koeshidayatullah et al., 2020) but has not yet been tested experimentally and numerically. Finally, the possibility that residual, undolomitized limestone has been leached after dolomitization, perhaps because of the contrast in reactivity between limestone and dolomite at the reaction front, cannot be completely ruled out. Whatever the controls, however, there is good evidence from this study and in the literature (e.g. Davies and Smith, 2006; Wendte, 2006; Hirani et al., 2018) that substantially higher volumes of effective porosity can occur at the margins of fault-controlled dolomite bodies than in their core. In this study, the phenomenon where higher porosity is preserved at the dolomitization front in the Mount Whyte Formation is interpreted to be associated with the progressive decrease in porosity inboard of the reaction front, caused by the increase in crystal size, and decrease in pore size during recrystallization in the core of the body.

6. Conclusion

This study shows, for the first time, that dolomite at a dolomite-limestone transition is non-stoichiometric and forms at cooler temperatures than inboard of the transition, within the core of the dolomite body. This is interpreted to reflect less recrystallization and stabilization of dolomite at the dolomite-limestone transition compared to the main dolomite bodies. As such, the dolomite-limestone transition is interpreted to represent an archive of the first (oldest) phase of dolomitization, which was then progressively recrystallized, closer to the fluid source. The non-stoichiometry of dolomite at the transition implies that the Mg/Ca ratio of the fluid governed the extent of dolomitization. Subsequent phases of dolomitization nucleated upon, and recrystallized these first-formed crystals, eventually resulting in overdolomitization. Consequently, porosity was occluded and the reaction front back-stepped towards the fluid source. Ultimately, this dynamic, self-limiting dolomitization model may help to explain a common phenomenon of higher porosity and permeability recorded at the termination of dolomite bodies. Therefore, once complete dolomitization and mineral stabilization are achieved, dolomite bodies will not increase in size, even if more Mg-rich fluids are introduced into the system, and dolomite precipitation will instead focus upon fault and fracture networks.

Declaration of competing interest

The authors declare that they have no known competing financial interests or personal relationships that could have appeared to influence the work reported in this paper.

Acknowledgements

This study is supported by the Presidential Doctoral Award for Ardiansyah Koeshidayatullah. Additional supports were provided through IAS and AAPG (Fred A. and Jean Dix Named Grant) student research grants. Fieldwork and analytical costs are partially funded by a NERC grant to Cathy Hollis and Adrian Boyce (IP-1759-1117). We thanked colleagues at the Williamson Research Centre, University of Manchester, Alberta Geological Survey and University of Miami for their great support. Kind support from Matthew MacInnis and Pillar Lecumberri-Sanchez at the University of Alberta on the fluid inclusion analysis are gratefully acknowledged. Constructive comments from Stefan Schroeder, David Budd and Juan Diego Martin-Martin have greatly improved the earlier version of the paper. We are grateful for the constructive criticism by the Earth and Planetary Science Letters editor, Itay Halevy, and Brian Jones and an anonymous reviewer.

Appendix A. Supplementary material

Supplementary material related to this article can be found online at https://doi.org/10.1016/j.epsl.2020.116291.

References

Al-Ramadan, K., Koeshidayatullah, A., Cantrell, D., Swart, P.K., 2019. Impact of basin architecture on diagenesis and dolomitization in a fault-bounded carbonate platform: outcrop analogue of a pre-salt carbonate reservoir, Red Sea rift, NW Saudi Arabia. Pet. Geosci. https://doi.org/10.1144/petgeo2018-125.

Amao, A.O., Al-Ramadan, K., Koeshidayatullah, A., 2016. Automated mineralogical methodology to study carbonate grain microstructure: an example from oncoids. Environ. Earth Sci. 75 (8), 666.

Budd, D.A., Mathias, W.D., 2015. Formation of Lateral Patterns in rock properties by dolomitization: evidence from a Miocene reaction front (Bonaire, Netherlands Antilles). J. Sediment. Res. 85 (9), 1082–1101.

Collom, C.J., Johnston, P.A., Powell, W.G., 2009. Reinterpretation of 'Middle' Cambrian stratigraphy of the rifted western Laurentian margin: Burgess Shale formation and contiguous units (Sauk II megasequence), Rocky Mountains, Canada. Palaeogeogr. Palaeoclimatol. Palaeoecol. 277 (1–2), 63–85.

Corbella, M., Gomez-Rivas, E., Martín-Martín, J.D., Stafford, S.L., Teixell, A., Griera, A., Travé, A., Cardellach, E., Salas, R., 2014. Insights to controls on dolomitization by means of reactive transport models applied to the Benicàssim case study (Maestrat Basin, eastern Spain). Pet. Geosci. 20 (1), 41–54.

Coto, B., Martos, C., Peña, J.L., Rodríguez, R., Pastor, G., 2012. Effects in the solubility of $CaCO_3$: experimental study and model description. Fluid Phase Equilib. 324, 1–7.

Davies, G.R., Smith Jr, L.B., 2006. Structurally controlled hydrothermal dolomite reservoir facies: an overview. Am. Assoc. Pet. Geol. Bull. 90 (11), 1641–1690.

Dennis, K.J., Affek, H.P., Passey, B.H., Schrag, D.P., Eiler, J.M., 2011. Defining an absolute reference frame for 'clumped' isotope studies of CO_2. Geochim. Cosmochim. Acta 75 (22), 7117–7131.

Gabrielse, H., 1991. Late Paleozoic and Mesozoic terrane interactions in North-central British Columbia. Can. J. Earth Sci. 28 (6), 947–957.

Goldstein, R.H., Reynolds, T.J., 1994. Systematics of Fluid Inclusions in Diagenetic Minerals. Society for Sedimentary Geology Short Course, vol. 31. 199 pp.

Gregg, J.M., Bish, D.L., Kaczmarek, S.E., Machel, H.G., 2015. Mineralogy, nucleation and growth of dolomite in the laboratory and sedimentary environment: a review. Sedimentology 62 (6), 1749–1769.

Grove, C., Jerram, D.A., 2011. jPOR: an ImageJ macro to quantify total optical porosity from blue-stained thin sections. Comput. Geosci. 37 (11), 1850–1859.

Hauck, T.E., Pană, D., DuFrane, S.A., 2017. Northern Laurentian provenance for Famennian clastics of the Jasper basin (Alberta, Canada): a Sm-Nd and U-Pb detrital zircon study. Geosphere 13 (4), 1149–1172.

Hirani, J., Bastesen, E., Boyce, A., Corlett, H., Eker, A., Gawthorpe, R., Hollis, C., Korneva, I., Rotevatn, A., 2018. Structural controls on non-fabric-selective dolomitization within rift-related basin-bounding normal fault systems: insights from the Hammam Faraun Fault, Gulf of Suez, Egypt. Basin Res. 30 (5), 990–1014.

Hollis, C., Bastesen, E., Boyce, A., Corlett, H., Gawthorpe, R., Hirani, J., Rotevatn, A., Whitaker, F., 2017. Fault-controlled dolomitization in a rift basin. Geology 45 (3), 219–222.

Honlet, R., Gasparrini, M., Muchez, P., Swennen, R., John, C.M., 2018. A new approach to geobarometry by combining fluid inclusion and clumped isotope thermometry in hydrothermal carbonates. Terra Nova 30 (3), 199–206.

Horita, J., 2014. Oxygen and carbon isotope fractionation in the system dolomite–water–CO_2 to elevated temperatures. Geochim. Cosmochim. Acta 129, 111–124.

Kaczmarek, S.E., Sibley, D.F., 2014. Direct physical evidence of dolomite recrystallization. Sedimentology 61 (6), 1862–1882.

Kaczmarek, S.E., Thornton, B.P., 2017. The effect of temperature on stoichiometry, cation ordering, and reaction rate in high-temperature dolomitization experiments. Chem. Geol. 468, 32–41.

Kaczmarek, S.E., Gregg, J.M., Machel, H.G., Fouke, B.W., Bish, D.L., 2017. Dolomite, Very-High Magnesium Calcite, and Microbes: Implications for the Microbial Model of Dolomitization. SEPM Special Publication, vol. 109, pp. 1–14.

Kim, S.T., O'Neil, J.R., 1997. Equilibrium and nonequilibrium oxygen isotope effects in synthetic carbonates. Geochim. Cosmochim. Acta 61 (16), 3461–3475.

Koeshidayatullah, A., Corlett, H., Stacey, J., Swart, P.K., Boyce, A., Whitaker, F., Robertson, H., Hollis, C., 2020. Evaluating new fault-controlled hydrothermal dolomitisation models: an insight from the Cambrian Dolomite, Western Canada sedimentary basin. Sedimentology. https://doi.org/10.1111/sed.12729.

Kondratiuk, P., Tredak, H., Ladd, A.J., Szymczak, P., 2015. Synchronization of dissolution and precipitation fronts during infiltration-driven replacement in porous rocks. Geophys. Res. Lett. 42 (7), 2244–2252.
Lumsden, D.N., 1979. Discrepancy between thin-section and X-ray estimates of dolomite in limestone. J. Sediment. Res. 49 (2), 429–435.
Lumsden, D.N., Morrison, J.W., Lloyd, R.V., 1995. The role of iron and Mg/Ca ratio in dolomite synthesis at 192 °C. J. Geol. 103 (1), 51–61.
Machel, H.G., 2004. Concepts and models of dolomitization: a critical reappraisal. In: Braithwaite, C.J.R., Rizzi, G., Darke, G. (Eds.), The Geometry and Petrogenesis of Dolomite Hydrocarbon Reservoirs. In: Geological Society (London) Special Publication, vol. 235, pp. 7–63.
Martín-Martín, J.D., Travé, A., Gomez-Rivas, E., Salas, R., Sizun, J.P., Vergés, J., Corbella, M., Stafford, S.L., Alfonso, P., 2015. Fault-controlled and stratabound dolostones in the Late Aptian–earliest Albian Benassal formation (Maestrat Basin, E Spain): petrology and geochemistry constrains. Mar. Pet. Geol. 65, 83–102.
Merino, E., Banerjee, A., 2008. Terra rossa genesis, implications for karst, and eolian dust: a geodynamic thread. J. Geol. 116 (1), 62–75.
Merino, E., Canals, À., 2011. Self-accelerating dolomite-for-calcite replacement: self-organized dynamics of burial dolomitization and associated mineralization. Am. J. Sci. 311 (7), 573–607.
Morrow, D.W., 1982. Diagenesis 2. Dolomite-part 2 dolomitization models and Ancient dolomites. Geosci. Can. 9 (2).
Nader, F.H., Swennen, R., Ellam, R.M., 2007. Field geometry, petrography and geochemistry of a dolomitization front (Late Jurassic, central Lebanon). Sedimentology 54 (5), 1093–1120.
Newport, R., Segura, M., Redfern, J., Hollis, C., 2020. The interaction of tectonics, climate and eustasy in controlling dolomitization: a case study of Cenomanian–Turonian, shallow marine carbonates of the Iberian basin. Sedimentology. https://doi.org/10.1111/sed.12704.
Olanipekun, B.J., Azmy, K., 2017. In situ characterization of dolomite crystals: evaluation of dolomitization process and its effect on zoning. Sedimentology 64 (6), 1708–1730.
Pană, D.I., van der Pluijm, B.A., 2015. Orogenic pulses in the Alberta Rocky Mountains: radiometric dating of major faults and comparison with the regional tectono-stratigraphic record. Geol. Soc. Am. Bull. 127 (3–4), 480–502.
Powell, W.G., Johnston, P.A., Collom, C.J., Johnston, K.J., 2006. Middle Cambrian brine seeps on the Kicking Horse Rim and their relationship to talc and magnesite mineralization and associated dolomitization, British Columbia, Canada. Econ. Geol. 101 (2), 431–451.
Pugh, D.C., 1973. Subsurface Lower Paleozoic Stratigraphy in Northern and Central Alberta, Vol. 72, No. 12. Department of Energy, Mines and Resources.
Putnis, A., 2009. Mineral replacement reactions. Rev. Mineral. Geochem. 70 (1), 87–124.
Roedder, E., 1984. Fluid Inclusions, vol. 12. Mineralogical Society of America.
Rosenbaum, J., Sheppard, S.M.F., 1986. An isotopic study of siderites, dolomites and ankerites at high temperatures. Geochim. Cosmochim. Acta 50 (6), 1147–1150.
Saller, A.H., Henderson, N., 1998. Distribution of porosity and permeability in platform dolomites: insight from the Permian of West Texas. Am. Assoc. Pet. Geol. Bull. 82 (8), 1528–1550.
Sharma, T., Clayton, R.N., 1965. Measurement of $O^{18}O^{16}$ ratios of total oxygen of carbonates. Geochim. Cosmochim. Acta 29 (12), 1347–1353.
Sharp, I., Gillespie, P., Morsalnezhad, D., Taberner, C., Karpuz, R., Vergés, J., Horbury, A., Pickard, N., Garland, J., Hunt, D., 2010. Stratigraphic architecture and fracture-controlled dolomitization of the Cretaceous Khami and Bangestan groups: an outcrop case study, Zagros Mountains, Iran. Geol. Soc. (Lond.) Spec. Publ. 329 (1), 343–396.
Shelton, K.L., Orville, P.M., 1980. Formation of synthetic fluid inclusions in natural quartz. Am. Mineral. 65 (11–12), 1233–1236.
Staudigel, P.T., Murray, S., Dunham, D.P., Frank, T.D., Fielding, C.R., Swart, P.K., 2018. Cryogenic brines as diagenetic fluids: reconstructing the diagenetic history of the Victoria Land Basin using clumped isotopes. Geochim. Cosmochim. Acta 224, 154–170.
Wendte, J., 2006. Origin of molds in dolomites formed by the dissolution of calcitic grains: evidence from the Swan Hills formation in West-central Alberta and other Devonian formations in Alberta and northeastern British Columbia. Bull. Can. Pet. Geol. 54 (2), 91–109.
Wilson, E.N., Hardie, L.A., Phillips, O.M., 1990. Dolomitization front geometry, fluid flow patterns, and the origin of massive dolomite: the Triassic Latemar buildup, northern Italy. Am. J. Sci. 290 (7), 741–796.
Wilson, M.E., Evans, M.J., Oxtoby, N.H., Nas, D.S., Donnelly, T., Thirlwall, M., 2007. Reservoir quality, textural evolution, and origin of fault-associated dolomites. Am. Assoc. Pet. Geol. Bull. 91 (9), 1247–1272.
Wright, G.N., McMechan, M.E., Potter, D.E.G., Mossop, G.D., Shetsen, I., 1994. Structure and Architecture of the Western Canada Sedimentary Basin. Geological Atlas of the Western Canada Sedimentary Basin, vol. 4, pp. 25–40.
Xiao, Y., Jones, G.D., 2007. Reactive transport models of limestone-Dolomite transitions: implications for reservoir connectivity. In: International Petroleum Technology Conference. International Petroleum Technology Conference.
Yapparova, A., Gabellone, T., Whitaker, F., Kulik, D.A., Matthäi, S.K., 2017. Reactive transport modelling of hydrothermal dolomitisation using the CSMP++ GEM coupled code: effects of temperature and geological heterogeneity. Chem. Geol. 466, 562–574.